Correspondence to:
D. D. Turner,
dave.turner@noaa.gov

Validating the Water Vapor Variance Similarity Relationship in the Interfacial Layer Using Observations and Large-Eddy Simulations

M. K. Osman[1,2], D. D. Turner[3] iD, T. Heus[4] iD, and V. Wulfmeyer[5] iD

[1]Cooperative Institute for Mesoscale Meteorological Studies, The University of Oklahoma, and NOAA/National Severe Storms Laboratory, Norman, OK, USA, [2]Now at Enable Midstream Partners, Oklahoma City, OK, USA, [3]Global Systems Division, NOAA Earth System Research Laboratory, Boulder, CO, USA, [4]Department of Physics, Cleveland State University, Cleveland, OH, USA, [5]Institute of Physics and Meteorology, University of Hohenheim, Stuttgart, Germany

Abstract In previous work, the similarity relationship for the water vapor variance in the interfacial layer (IL) at the top of the convective boundary layer (CBL) was proposed to be proportional to the convective velocity scale and the gradients of the water vapor mixing ratio and the Brunt-Vaisala frequency in the entrainment zone. In the presence of wind shear in the IL, the similarity relationship was hypothesized to also include a dependence on the gradient Richardson number. Simultaneous measurements of the surface buoyancy flux, wind-shear profiles from a radar wind profiler, water vapor mixing ratio and temperature measurements and their gradients from a Raman lidar provide a unique opportunity to thoroughly examine the function used in defining the variance and validate it. These observations were made over the Atmospheric Radiation Measurement Southern Great Plains site. We identified 19 cases from 2016 during which the CBL was quasi-stationary and well mixed for at least 2 hr in the afternoon. Furthermore, we simulated the CBL using a large-eddy simulation (LES) model for these cases and derived the water vapor variance and other profiles to test the similarity function. Utilizing this unique combination of observations and LES, we demonstrate that the water vapor variance in the IL has little-to-no dependence on wind shear. Furthermore, we demonstrate that the predicted variance using the original similarity function matches the observed and LES-modeled variance very well, with linear correlations between the two variances of 0.82 and 0.95, respectively.

Plain Language Summary Numerical weather prediction and global circulation models need to be able to predict the variance in water vapor in the atmosphere, as this is an important signature of turbulent mixing. However, the variance is something that is not directly resolved by the model and must be approximated using variables that the models actually resolve such as gradients in water vapor, temperature, and wind. This study evaluates a commonly used approximation approach, illustrates its shortcomings, and suggests how the approximation can be improved.

1. Introduction

The convective boundary layer (CBL) is the layer in the lower troposphere that is in contact with the ground and is directly influenced by the Earth's surface. The CBL is further divided into three regimes known as surface layer, mixed layer, and the interfacial layer (IL). The surface layer, which is the lowermost portion of the CBL, can be described in terms of the Monin-Obukhov similarity theory, which relates the vertical gradients in temperature, humidity, and wind to surface fluxes and stability functions given for different ranges of the bulk Richardson number (e.g., Grachev et al., 2000; Jiménez et al., 2012; Poulos et al., 2002). The mixed layer is the central portion of the CBL where the vertical profiles of water vapor mixing ratio, conserved tracers, and potential temperature are nearly constant. The IL is defined as the interface between the top of the CBL and the free troposphere that separates the turbulent boundary layer from the less turbulent free troposphere.

The IL plays a vital role for the diurnal evolution of the CBL as well as for the exchange of heat, mass, and momentum between the CBL and the free troposphere. Such turbulent transport is crucial for both the horizontal and vertical distribution of scalars such as water vapor and other constituents, as well as for the vertical stability of the IL. An exact quantification of the entrainment fluxes and boundary layer's budgets is critical for improving our understanding of the dynamic and thermodynamic evolution of the CBL.

Turbulent processes act at resolutions much finer than the grid sizes used in virtually all climate and weather prediction models. Thus, these processes must be parameterized using variables that are actually resolved by these models (e.g., vertical profiles in scalars, temperature, and wind). The proper representation of turbulent vertical exchange between the CBL and the free troposphere in general circulation, numerical weather prediction, and other numerical models is required in order to improve their predictive capacity; examples of some of these turbulent boundary layer schemes used in weather and climate models include the updated Mellor-Yamada-Nakanishii-Niino (Angevine et al., 2018; Nakanishi & Niino, 2009) and Cloud Layers Unified by Bimodals (Golaz et al., 2002) schemes.

Entrainment processes can be studied using both observations and numerical simulations. Both observations (e.g., Berg et al., 2017; Couvreux et al., 2007; Mahrt, 1991) and numerical simulations (e.g., Deardorff, 1974; Mellado et al., 2017) have offered significant insights into the moisture distribution and transport around the IL. For example, it is known that dry air from the free atmosphere can penetrate deep into the CBL, resulting in a negative skewness or third-order moment of the water vapor mixing ratio near the top of the CBL, whereas the penetration of convective eddies above the CBL top results in a positive skewness or third-order moment (e.g., Couvreux et al., 2007; Mellado et al., 2017; Osman et al., 2018; Turner, Wulfmeyer, et al., 2014; Wulfmeyer et al., 2016). This deep dry entrainment can also affect the water vapor budget and variance at the surface (e.g., Santanello et al., 2018; Simmer et al., 2015).

A large number of researchers have used large-eddy simulation (LES) models to establish a better understanding of the mixing processes at work in the IL and its impact on the CBL (e.g., Conzemius & Fedorovich, 2006; Garcia & Mellado, 2014; Gentine et al., 2015; Liu et al., 2018; Mellado et al., 2017). In particular, Sorbjan used his LES model (Sorbjan, 1996) to conclude that the water vapor variance in the IL could be described in terms of the convective velocity scale, the gradient of water vapor mixing ratio, and the Brunt-Vaisala frequency (Sorbjan, 2005, 2006). Furthermore, he added a hypothesis for the dependence of the water vapor variance on wind shear, or equivalently the gradient Richardson number, in the IL. An overview of these relationships is presented in Wulfmeyer et al. (2016). If these relationships are correct, they can serve as a basis for advanced versions of turbulence parameterizations in mesoscale models.

However, a thorough validation of these relationships using observational data is missing. Turner, Wulfmeyer, et al. (2014) and Osman et al. (2018) used multiyear remote sensing data to look at water vapor variance in the IL and CBL, but the insight was limited because these data sets did not include wind shear and temperature gradients. Wulfmeyer et al. (2016) discussed how a new generation of water vapor Raman lidar, Doppler lidar, and wind profiler instruments, if all collocated at one site, could be used to evaluate these similarity relationships in the IL.

Here, we present—what is to our knowledge—the first observationally based evaluation of the similarity relationships with respect to water vapor variance in the IL. This evaluation was performed at the Atmospheric Radiation Measurement (ARM) Southern Great Plains (SGP) site in north central Oklahoma (Sisterson et al., 2016). This site has the required instrument synergy that provides simultaneous measurements of water vapor variance and its gradient, as well as measurements of the wind shear and temperature gradient profiles in the IL.

2. Water Vapor Variance Similarity Relationships in the IL

Sorbjan (1996, 2001, 2005, 2006) worked to define similarity relationships to predict variances and fluxes in the IL. These equations were summarized in Wulfmeyer et al. (2016); however, they are reproduced here (equations (1)–(4)) for the sake of completeness and simplify the discussion. Sorbjan hypothesized that turbulent moments and fluxes should be dependent on the following scaling variables

$$S_w = w_* \tag{1}$$

$$S_L = \frac{w_*}{N_I} \tag{2}$$

$$S_q = S_L g_I = w_* \frac{g_I}{N_I} \tag{3}$$

$$S_\theta = S_L \gamma_I = w_* \frac{\gamma_I}{N_I} \tag{4}$$

where S_w, S_L, S_q, and S_θ are the scaling variables for vertical velocity (w), the IL length scale (L), the water vapor mixing ratio (q), and potential temperature (θ), respectively. Note that the Deardorff convective velocity scale w_* is given by

$$w_* = \left(\frac{g}{\overline{\theta}_v} z_i H_o \right)^{1/3} \tag{5}$$

where g is the acceleration due to gravity, $\overline{\theta}_v$ is the mean virtual potential temperature within the CBL, z_i is the depth of the CBL, and H_o is the surface buoyancy flux. Here, g_I is the vertical gradient of water vapor mixing ratio at z_i and is expressed as

$$g_I = \left. \frac{d\overline{q}}{dz} \right|_{z_i}. \tag{6}$$

N_I is the Brunt-Vaisala frequency in the IL and is given by

$$N_I = \sqrt{\frac{g}{\overline{\theta}} \left. \frac{d\overline{\theta}}{dz} \right|_{z_i}} \tag{7}$$

where $\left. \frac{d\overline{\theta}}{dz} \right|_{z_i} = \gamma_I$ is the potential (virtual) temperature gradient in the IL. Note that the overbar on q and θ in the equations above denotes averages over the 2-hr sampling period.

Wulfmeyer et al. (2016) summarized the similarity relationships proposed by Sorbjan between these scaling variables and both water vapor variance $\overline{q'^2_I}$ and water vapor vertical flux Q_I as

$$\overline{q'^2_I} = C_{q^2} S_q^2 f_{q^2}(R_I) = C_{q^2} w_*^2 \left(\frac{g_I}{N_I} \right)^2 f_{q^2}(R_I) \tag{8}$$

$$Q_I = -C_Q S_w S_q f_Q(R_I) = -C_Q w_*^2 \left(\frac{g_I}{N_I} \right) f_Q(R_I) \tag{9}$$

where C_x are positive constants and could be different for the water vapor variance versus water vapor vertical flux, and f_{q^2} and f_Q are functions of the gradient Richardson number R_I. R_I is a function of the Brunt-Vaisala frequency and the wind shear S_I in the IL and is defined as

$$R_I = \frac{N_I^2}{S_I^2}. \tag{10}$$

The wind shear in the IL is defined as

$$S_I^2 = \left(\left. \frac{d\overline{U}}{dz} \right|_{z_i} \right)^2 + \left(\left. \frac{d\overline{V}}{dz} \right|_{z_i} \right)^2, \tag{11}$$

where $\overline{U}$ and $\overline{V}$ are mean zonal and meridional winds over the 2-hr sampling period, respectively.

Sorbjan hypothesized that if the CBL was shearless, then the similarity relationship in equation (8) would reduce to

$$\overline{q'^2_I} = C_{q^2} w_*^2 \left(\frac{g_I}{N_I} \right)^2 \tag{12}$$

Figure 1. The Atmospheric Radiation Measurement Southern Great Plains central facility site, showing the location of the Raman lidar and Doppler lidar (red), 915 MHz radar wind profiler (blue), eddy covariance station (yellow), and energy balance Bowen ratio station (green). The distance between the Raman lidar and ECOR station is 95 m, whereas the distance between the Raman lidar and EBBR station is 170 m. The photos are courtesy of Google Earth and DD Turner.

However, if the boundary layer was experiencing forced convection (i.e., $S_I \gg 0$), Sorbjan's LES results suggested that the water vapor variance seemed to increase as R_I decreased and vice versa. He hypothesized that this dependence on the gradient Richardson number could be described by

$$f_{q^2}(R_I) = \frac{1 + {}^{c_r}/_{R_I}}{1 + {}^{1}/_{R_I}}$$

(13)

where c_r is a positive constant. This function (equation (13)) is bounded between 1 (when R_I approaches infinity) and c_r (when R_I approaches 0). Thus, using equation (13) in equation (8) is the same as equation (12) in the shearless environment.

Sorbjan (2006) derived $C_{q2} = 0.08$ and $c_r = 8$ from his analysis; however, there are significant uncertainties in these constants. Furthermore, Sorbjan cautioned that the uncertainty in his LES results associated with numerical effects, resolution, and subgrid parameterization could impact his determination of the functional form of the gradient Richardson number (equation (13)). (Sorbjan also provided an estimate for C_Q, but due to the complexities of merging Raman lidar moisture and Doppler lidar vertical motions together to derive water vapor flux profiles, we will limit our subsequent discussion to only the water vapor variance.)

The similarity relationships shown here (equations (8), (12), and (13)) contain a large number of assumptions and, to our knowledge, have not been directly evaluated with observations. The SGP site in north central Oklahoma (36.606°N, 97.485°W) has a wide range of instrumentation and is able to observe all of the geophysical variables needed to evaluate these similarity relationships. Furthermore, LES models have advanced significantly in the last decade, and we will use very high vertical resolution simulations to provide an additional evaluation of these similarity relationships.

3. Observations and LES Model

To evaluate the similarity relationship provided in equation (8), we need observations of $\overline{q_I'^2}$, g_I, γ_I (which is equivalent to N_I), S_I, and w_*. The first three variables are observed by the Raman lidar, the shear by the 915-MHz wind profiler, and the last by the surface energy balance station. Additionally, we specify z_i as the height where the water vapor variance has its maximum, following Turner, Wulfmeyer, et al. (2014). The locations of these instruments at the SGP Central Facility are shown in Figure 1. The instruments are located within 170 m of each other, and thus can be assumed to be collocated. The ARM site also has a Doppler lidar

that could be used to observe the wind shear. However, the Doppler lidar system deployed at the SGP site in 2016 was underpowered and did not observe the IL well, hence our decision to use the 915 MHz wind profiler to derive S_I (note Berg et al. (2017) used the radar wind profiler instead of the Doppler lidar to measure this variable for the same reason).

To complement the observational analysis, we simulated the evolution of the CBL using a LES model. The observed data and LES output were analyzed in an identical manner to evaluate the accuracy of the similarity relationship in reproducing the water vapor variance in the IL.

3.1. Raman Lidar

The Raman lidar was designed and built specifically for the ARM program to measure profiles of water vapor mixing ratio (Turner et al., 2016). The original system, which was deployed in 1995 and described by Goldsmith et al. (1998), was upgraded significantly in 2004 which allowed it to observe water vapor profiles at 10-s resolution (Ferrare et al., 2006; Turner et al., 2016). The Raman lidar transmits 350-mJ pulses of 355-nm light at 30 Hz into the atmosphere, and the backscattered energy is collected by a 61 cm diameter telescope. Dichroic optics are used to separate the elastic return at 355 nm from aerosols and molecules from the Raman scattered returns from nitrogen (387 nm) and water vapor (408 nm) molecules. The upgraded system uses detection electronics that combine both analog-to-digital and photon counting technologies to observe the backscattered return as a function of time; the temporal resolution of these electronics is fast enough to provide 7.5 m vertical resolution (Newsom et al., 2009). To improve the signal-to-noise ratio, the data are summed to provide 60 m vertical resolution, but the 10-s temporal resolution is maintained.

Wulfmeyer et al. (2010) first demonstrated that the 10-s Raman lidar water vapor observations have sufficient signal-to-noise that the second (variance) and third moment of the water vapor mixing ratio could be observed. Turner, Ferrare, et al. (2014) demonstrated that the water vapor variance and skewness observed by the Raman lidar agreed well with in situ measurements made by aircraft. Turner, Wulfmeyer, et al. (2014) identified 300 cases in the middle-to-late afternoon when the CBL was well developed between 2005 and 2011, and analyzed the Raman lidar water vapor data to derive the first observationally derived water vapor variance and skewness "climatology."

We used the same approach specified in Turner, Wulfmeyer, et al. (2014) to derive $\overline{q_I'^2}$ over a 2-hr period when the CBL is quasi-stationary. This included using the split-histogram approach developed by McNicholas and Turner (2014) to identify outliers before the variance was computed at each level using the Lenschow et al. (2000) method. We take the 10-min averaged water vapor mixing ratio data (which is the standard ARM data product) and averaged it over our 2-hr analysis period (the selection of these periods is described in section 4.1 below) to get the profile of water vapor mixing ratio with height, from which g_I is derived using equation (6). Note that the vertical resolution of the water vapor data used in this study was 60 m.

As part of the upgrade in 2004, additional detection channels sensitive to the rotational Raman scattering by nitrogen and oxygen were added to the Raman lidar thereby enabling it to profile temperature (Newsom et al., 2013; Turner et al., 2016). Unfortunately, the signal-to-noise is not high enough to measure temperature profiles at 10-s resolution, and thus we are unable to evaluate the higher moments of temperature. However, we are able to derive a mean temperature profile over our 2-hr analysis period, from which γ_I and hence N_I can be computed (equation (7)). The vertical resolution of the temperature data was 75 m.

3.2. The 915 MHz Wind Profiler

A 915 MHz radar wind profiler was used to measure the wind shear in the IL (i.e., S_I). The profiler uses fixed beams pointing vertically and off vertically and is designed to measure wind in the boundary layer and free troposphere (Ecklund et al., 1988; Williams et al., 1995). The wind profiler operates by transmitting electromagnetic energy into the atmosphere and then gathering the information from the returned backscattered radar power due to inhomogeneities of the refractive index of the atmosphere. The recorded measurements are analyzed to generate winds at temporal and vertical resolutions of 10 min and 62.5 m, respectively. For this study, the data were averaged over the 2-hr time periods used for the Raman lidar data analyses.

3.3. Surface Energy Budget Station

The SGP site has two types of surface energy balance stations at its Central Facility: an eddy covariance (ECOR; Atmospheric Radiation Measurement (ARM), 1997) station and an energy balance Bowen ratio

Table 1
The Data for the 19 Cases Used in This Analysis

			Observations					LES output				
Day	Time	z_i	$\overline{q_I'^2}$	g_I	N_I^2	S_I^2	w_*	$\overline{q_I'^2}$	g_I	N_I^2	S_I^2	w_*
		(km)	(g²/kg²)	(g·kg⁻¹·m⁻¹)	(s⁻²)	(s⁻²)	(m/s)	(g²/kg²)	(g·kg⁻¹·m⁻¹)	(s⁻²)	(s⁻²)	(m/s)
0216	1900	1.335	0.575	−0.007	0.000404	0.001150	2.191	0.096	−0.004	0.000210	0.000448	2.357
0216	2100	1.275	0.518	−0.009	0.000237	0.000603	1.697	0.082	−0.003	0.000146	0.000387	2.363
0216	2300	1.305	0.451	−0.008	0.000217	0.000250	1.072	0.057	−0.003	0.000129	0.000218	1.826
0220	2130	0.915	0.397	−0.018	0.000645	0.000608	1.270	0.204	−0.011	0.000531	0.000017	2.261
0222	2230	1.215	0.324	−0.012	0.000202	0.000144	0.990	0.151	−0.006	0.000335	0.000386	2.079
0301	2230	1.155	0.219	−0.005	0.000166	0.000303	1.245	0.037	−0.002	0.000153	0.000356	1.713
0415	1930	1.335	1.450	−0.025	0.000366	0.000011	1.831	0.388	−0.013	0.000443	0.000032	2.167
0415	2300	1.425	0.823	−0.025	0.000578	0.000513	0.760	0.284	−0.019	0.000679	0.000312	1.485
0422	2100	1.215	0.724	−0.017	0.000175	0.000076	1.551	0.374	−0.008	0.000175	0.000177	2.127
0430	2200	1.215	0.444	−0.009	0.000461	0.001603	1.427	0.325	−0.019	0.000833	0.000150	1.808
0615	1915	1.695	8.790	−0.034	0.000141	0.000053	2.277	3.260	−0.013	0.000144	0.000004	2.615
0617	2230	2.115	6.019	−0.031	0.000486	0.000196	1.833	1.270	−0.005	0.000058	0.000062	2.500
0721	2230	2.385	4.558	−0.018	0.000220	0.000069	2.251	0.987	−0.006	0.000090	0.000009	2.457
0722	1900	2.385	3.617	−0.015	0.000296	0.000032	2.691	0.539	−0.002	0.000058	0.000068	2.567
0722	2100	2.505	4.184	−0.012	0.000294	0.000031	2.532	1.380	−0.007	0.000111	0.000019	2.702
0722	2300	2.505	3.333	−0.019	0.000205	0.000083	1.986	1.390	−0.008	0.000135	0.000014	2.435
0821	1845	1.965	1.055	−0.013	0.000478	0.000318	2.534	0.584	−0.007	0.000194	0.000179	2.690
0822	2100	2.025	4.445	−0.028	0.000505	0.000132	2.487	1.110	−0.012	0.000272	0.000051	2.553
0822	2300	1.935	2.805	-0.032	0.000587	0.000160	1.828	1.490	−0.018	0.000346	0.000198	2.296

Note. The day is formatted as MMDD, where MM is the month and DD is the day of the month (all data from 2016). The time listed is the center of the averaging period and is formatted as HHMM, where HH is the hour and MM is the minute. All times are UTC and represent the middle of the 2-hr processing window. LES = large-eddy simulation.

(EBBR; Atmospheric Radiation Measurement (ARM), 1993) station. Both systems provide measurements of the latent and sensible heat fluxes from the surface. The ECOR uses a fast-response, 10-Hz, three-dimensional sonic anemometer located 2 m above the land surface (and 95 m west of the Raman lidar) to record the three components of the wind and the air temperature, and an open path infrared gas analyzer to obtain water vapor density. These measurements are processed using the eddy covariance technique to generate turbulent fluxes of momentum, sensible heat, and latent heat at 30-min resolution (e.g., Kaimal & Finnigan, 1994). The EBBR system computes latent and sensible heat fluxes using the Bowen ratio approach described in Brutsaert (1982), where the Bowen ratio is measured using the ratio of the gradients of temperature and water vapor pressure observed between two fixed heights below 3 m. At the SGP Central Facility, the ECOR system is positioned to sample a farm field, whereas the EBBR station is used to sample a pasture (Figure 1). For this study, the buoyancy flux from each system was averaged over 2-hr time window used for the other data (described in section 4.1). We derived w_* using equation (5) by combining the buoyancy flux measurements from these energy balance systems with z_i determined from the Raman lidar as indicated above. The following results using the w_* derived from the ECOR and EBBR stations were in very good agreement with each other, and thus we only show results from the ECOR station below.

3.4. LES Model

The observational analysis has been supplemented using a LES model to simulate the CBL for the same selected cases, and we use the LES output to test the similarity function also. In comparison with previous studies (such as Sorbjan, 2005, 2006), modern computing power allows us to (1) run the LES at a higher resolution to better resolve the IL, and (2) run more cases than just six to span up a larger part of the phase space. Further, running simulations that match the days that were selected in the observational analysis means that observations and computations could better complement each other.

The LES simulations were carried out using the MicroHH model (van Heerwaarden et al., 2017) for the same dates as used for the observation cases (Table 1). MicroHH is a computational fluid dynamics code that is
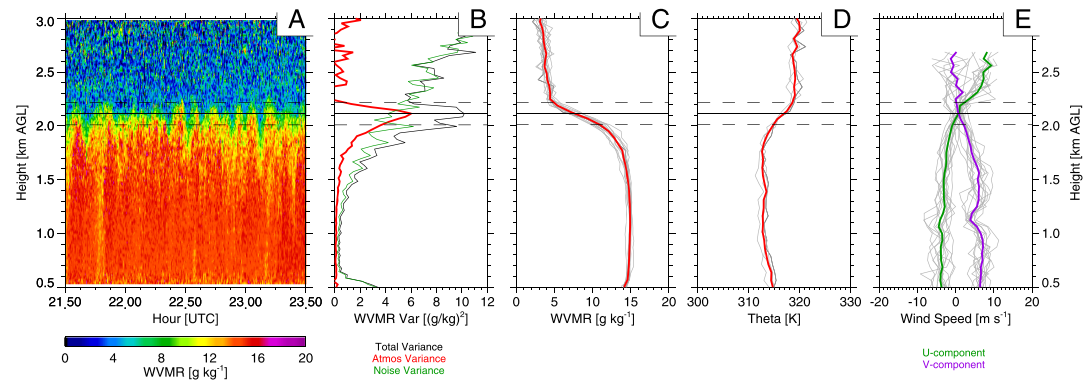
Figure 2. Data from 17 June 2016 from 2130 to 2330 UTC, showing (a) the time-height of the 10-s water vapor mixing ratio, (b) the profile of water vapor variance (red), instrument noise variance (green), and total variance (black), (c, d) the mean water vapor mixing ratio and potential temperature profiles in red with the 10- and 30-min profiles that were used to derive these means shown in gray, and (e) the mean u (green) and v (purple) wind profiles. The solid horizontal line is z_i, and the two dashed lines denote the *FWHM* range of the water vapor variance around z_i.

able to simulate atmospheric motions using direct numerical simulation and LES approaches. This model has been designed to run on graphical processing units (GPUs), making it computationally fast. The boundary and initial conditions were derived using the ARM variational analysis approach described in Xie et al. (2004). The surface fluxes, which were based on observations, were fixed and homogeneous, and hence no vegetation feedback. Cyclic horizontal boundary conditions were used.

The simulations run with a horizontal and vertical resolution of 25 and 10 m, respectively, and a horizontal domain size of 12.8 km by 12.8 km. Each simulation starts and stops at 0600 and 1900 local time, respectively. The profiles of water vapor mixing ratio variance, the mean profiles of water vapor, temperature, and wind, and the mean surface buoyancy flux were calculated spatially, and then evaluated over the same 2-hr period as the observations. Therefore, these are averages over the domain whereas the lidar and radar profiles were local averages in time. Even though we present the results for 10 m vertical resolution simulations, additional simulations were run at 50 m vertical resolution to test the sensitivity of our results to the model's resolution. The results obtained from the two resolutions were found to be very similar to each other, and thus only the 10-m results are shown here.

4. Analysis

4.1. Case Selection

The remote sensors at the SGP site provide time-series observations, and thus we have to assume Taylor's frozen turbulence hypothesis to convert time-series into spatial statistics (i.e., that the contribution to the turbulence intensity from advection is negligible). Furthermore, the length of the time series needs to be sufficiently long to reduce the sampling error. This requires that the turbulent nature of the CBL does not change over this sampling period. We have used the same approach outlined in Turner, Wulfmeyer, et al. (2014) and Osman et al. (2018), wherein we searched for periods of 2 h in length where the CBL was quasi-stationary (i.e., z_i was constant throughout the period, there were no apparent synoptic boundaries passing over the site, etc.) for our analysis. We were also restricted to cases when (a) all of the instrument systems were collecting good data, (b) the atmospheric variance in the IL was at least 30% of the total variance at that level observed by the Raman lidar (i.e., that the random noise in the variance observations was not too large—this is the same approach used in Turner, Wulfmeyer, et al., 2014), (c) that the variational analysis data set used to drive the LES model was available, (d) that the sensible heat flux observed by the ECOR station was positive, and (e) the cumulus cloud fraction (as detected using the Raman lidar backscatter profiles) was less than 5% during the analysis period. This resulted in the identification of 19 cases in 2016 (Table 1).

An example of the case from 17 June 2016 is shown in Figure 2. The high temporal resolution water vapor measurements clearly show rising plumes of moist air and dry descending plumes at the top of the CBL
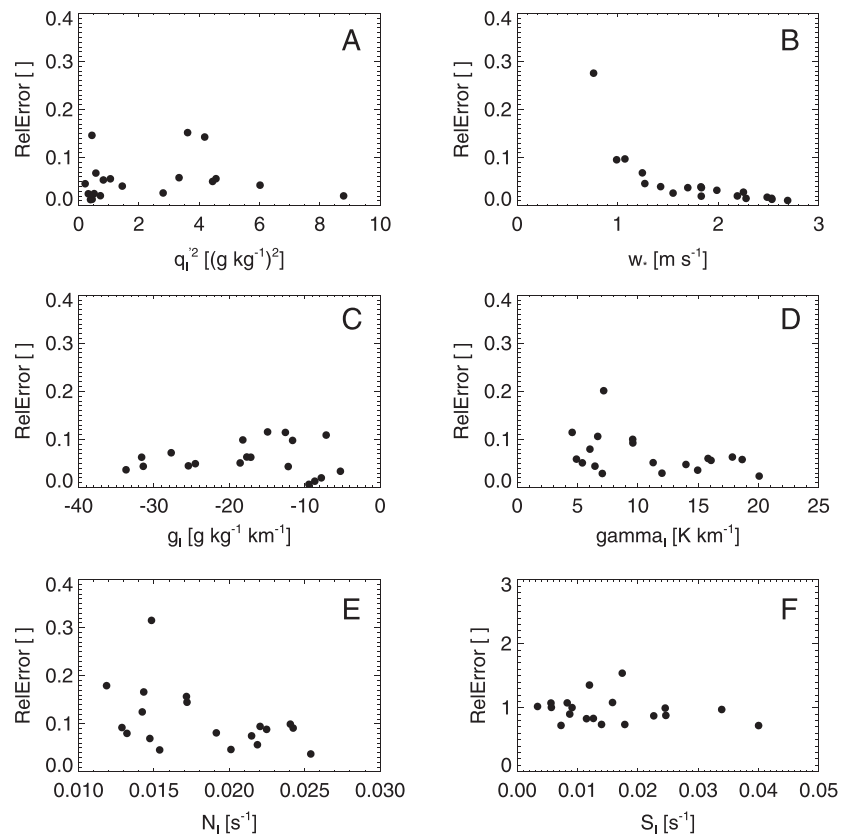
Figure 3. The relative uncertainty of the observed (a) water vapor variance, (b) convective velocity scale, (c) water vapor gradient, (d) potential temperature gradient, (e) Brunt-Vaisala frequency, and (f) wind shear for the 19 cases used in this analysis.

(Figure 2a). The total variance in the observed time series at each height was separated into atmospheric and instrumental variance (Figure 2b). The mean water vapor, temperature, and wind profiles are shown in Figures 2c–2e, respectively, and all show the expected gradients at the top of the CBL. The mean height of the CBL was determined from the peak in the water vapor variance profile (the same approach used in Turner, Wulfmeyer, et al., 2014), and the full-width half-maximum (*FWHM*) range of the water vapor variance peak around z_i was derived. The z_i and FWHM heights are shown by the horizontal solid and dashed lines, respectively. The gradients in the mean water vapor, mean temperature, and mean vector wind profiles (i.e., g_I, γ_I, and S_I) were determined over the FWHM layer.

All observations have uncertainties, and frequently, the magnitude of these uncertainties depends on the conditions of the measurement. The uncertainties in our observations, expressed as a relative error, are shown in Figure 3. The relative uncertainties in $\overline{q_I'^2}$, w_*, g_I, γ_I, and N_I are all generally 20% or smaller. However, the uncertainty in S_I is much larger and ranges from about 50% to 150%. This large uncertainty in the shear, which can be seen in the increased scatter of the individual profiles in Figure 2e, results in an average relative uncertainty in R_I of 200%.

4.2. Results

Similarity relationships provide a way to predict variables that are not directly prognosed by larger-scale models (such as higher order moments and fluxes) from variables that the model is able to predict (like gradients). Thus, as a starting point, we looked at the correlation between of $\overline{q_I'^2}$ and g_I^2, N_I^2, S_I^2, and w_*^2. These scatter plots, including both the observed and LES data, are shown in Figure 4, and the Pearson correlation coefficients (r) are given in Table 2.
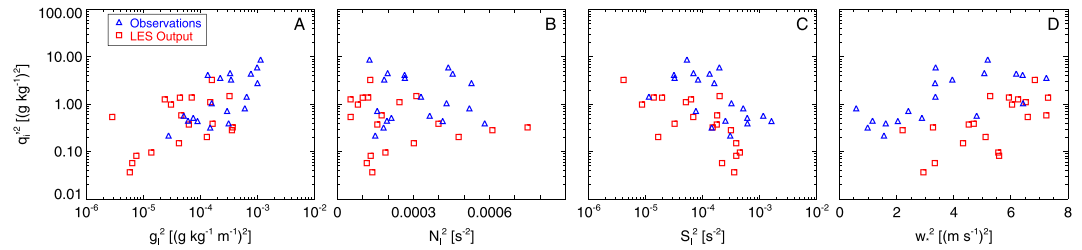
AGU
100
ADVANCING EARTH
AND SPACE SCIENCE

Journal of Geophysical Research: Atmospheres

10.1029/2019JD030653

Figure 4. The water vapor variance at z_i as a function of (a) the square of the gradient of water vapor mixing ratio at z_i, (b) the square of the Brunt-Vaisala frequency at z_i, (c) the square of wind shear at z_i, and (d) the square of the convective velocity scale from observations (blue triangles) and large-eddy simulation model (red squares). The observed w_* values shown here were computed from ECOR surface flux observations.

The correlation coefficient between $\overline{q_I'^2}$ and g_I^2 is 0.70 for the observation data in this study, which is in good agreement with previous observational studies at the SGP (Turner, Wulfmeyer, et al., 2014, where $r = 0.67$) and the ARM Darwin (Osman et al., 2018, where $r = 0.83$) sites. The correlation between these two variables in the LES output is markedly smaller ($r = 0.16$), which may be related to the much smaller water vapor gradient values in the LES output relative to the observational data (see Figure 4a). It is possible that the smaller water vapor vertical gradient values seen in the LES results relative to the observations are associated with biases (e.g., free troposphere is too wet, too little subsidence) in the data sets used to drive the LES model. However, the dynamic range of N_I^2, S_I^2, and w_*^2 are very similar for the LES and observations, and perhaps correspondingly, the correlation coefficients between these variables and $\overline{q_I'^2}$ are very similar between the LES and observations (Table 2).

We then evaluated the similarity relationship proposed by Sorbjan; namely, to see if the variance predicted by equation (8) using the function of the gradient Richardson number in equation (13) (and Sorbjan's coefficients for C_{q2} and c_r) matched the true water vapor variance. These results are shown in Figure 5. Note that the large uncertainties in the variance predicted by the similarity relationship is due to the uncertainty in R_I. (The uncertainty in R_I was computed by propagating the uncertainties of the shear and Brunt-Vaisala frequency; note that the uncertainty in the shear is the dominant term.) The water vapor variance computed by the similarity relationship is in reasonable agreement with the true variance, with linear correlation coefficients of 0.79 and 0.63. We also computed the correlation coefficient of the log of the true versus predicted variance, as this more equally weights the smaller values of variance in the calculation and resulted in a correlation coefficient of 0.85 and 0.84 for the observations and LES, respectively (Table 3).

We wanted to confirm that the correction for the gradient Richardson number (i.e., the specification of $f_{q2}(R_I)$ in equation (13)) matched the observation and LES output well, as this seemed to be the most uncertain aspect of Sorbjan's analysis. By rearranging equation (8), $f_{q2}(R_I)$ can be isolated as

$$f_{q^2}(R_I) = \frac{\overline{q_I'^2}}{C_{q^2}w_*^2\left(\frac{g_I}{N_I}\right)^2}. \tag{14}$$

We will refer to the right-hand side of equation (14) as the dimensionless variance ratio. We have all of the needed values to evaluate this relationship and have plotted the dimensionless variance ratio by gradient Richardson number in Figure 6 for both the observations and the LES output. Again, this figure uses the coefficients specified by Sorbjan. Two things were readily apparent: (1) The true variance is approximately 1 order of magnitude larger than the variance predicted by the similarity relationship, and (2) equation (13) using $c_r = 8$ does not describe the dependence on R_I very well. Thus, there is room for improvement in both of these areas.
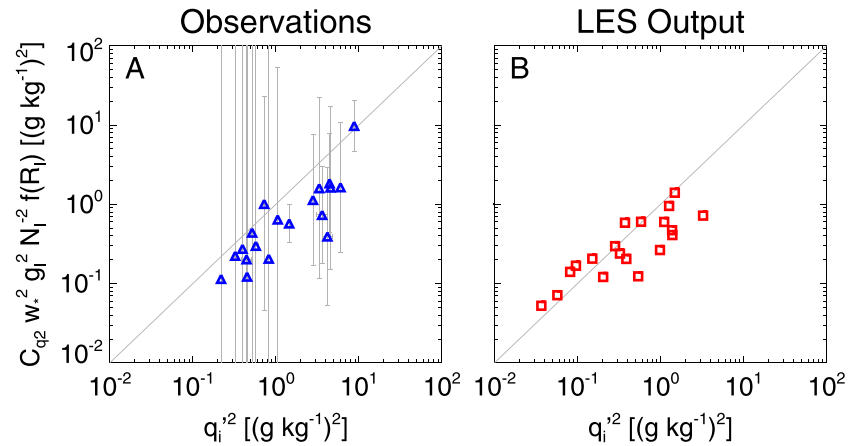
Table 2

The Linear Correlation Coefficients ("Lin x, Lin y") and Log-Log Correlation Coefficients ("Log x, Log y") Between $\overline{q_I'^2}$ and Other Variables Shown in Figure 4 for Both the Observations and the LES Output

	g_I^2	N_I^2	S_I^2	w_*^2
Observations (Lin x, Lin y)	0.70	−0.14	−0.46	0.59
LES output (Lin x, Lin y)	0.16	−0.28	−0.58	0.57
Observations (Log x, Log y)	0.71	0.01	−0.60	0.69
LES Output (Log x, Log y)o	0.49	−0.20	−0.70	0.61

Note. LES = large-eddy simulation.

Figure 5. Comparison of the computed versus true water vapor variance for the observations (left panel) and large-eddy simulation (LES; right panel), where the computed variance used the original Sorbjan coefficients $C_{q2} = 0.08$ and $c_r = 8$ in the similarity relationship given by equations (8) and (13). The correlation coefficients for both the observations and large-eddy simulation (LES) output is given in Table 3. The uncertainties in the observations are denoted with gray error bars.

To address the first problem, we modified the value of C_{q2} to 0.55, which was the median of the dimensionless variance ratio from the observations. However, it was not immediately clear how to improve the functional form of $f_{q^2}(R_I)$ to fit the data better; indeed, the results in Figure 6 seemed to suggest that there was no dependence on the gradient Richardson number at all (i.e., that setting $f_{q^2}(R_I)$ to a constant of 1 would be sufficient). If true, this would imply that the variance is not impacted by wind shear in the IL.

This line of thought, however, assumed that the functional form of the similarity relationship given by equation (8) is correct. If we assume that wind shear is important (as suggested by the nonnegligible correlation coefficients in Table 2), we could replace N_I^2 with S_I^2 to yield another possible relationship to predict the variance:

$$\overline{q_I'^2} = C_{q^2} w_*^2 \left(\frac{g_I}{S_I}\right)^2 f_{q^2}(R_I) \tag{15}$$

Note that the units are entirely consistent. To evaluate this hypothesis, we again rearranged the equation to isolate $f_{q^2}(R_I)$ to yield

$$f_{q^2}(R_I) = \frac{\overline{q_I'^2}}{C_{q^2} w_*^2 \left(\frac{g_I}{S_I}\right)^2}. \tag{16}$$

Figure 7 shows the dimensionless variance ratio given by the right side of equation (16) versus R_I. The dimensionless variance ratio for both the observed data and the LES output show a strong dependence on the gradient Richardson number. The function $f_{q^2}(R_I) = c\, R_I^{-1}$ fits both the observations and the LES output well (although the coefficient c was different for the two; 1.11 for the observations and 0.86 for the LES data). Updating equation (15) with this functional form for $f_{q^2}(R_I)$ and substituting in equation (10) yields

Table 3
The Correlation Coefficients for the Data Shown in Figures 5, 7, and 8, Computed Both the Correlation of the Actual Values ("Lin x, Lin y") and the Correlation of the Log of Each ("Log x, Log y")

		Observations	LES output
Figure 5	Lin x, Lin y	0.79	0.63
	Log x, Log y	0.85	0.84
Figure 7	Lin x, Lin y	−0.35	−0.43
	Log x, Log y	−0.93	−0.95
Figure 8	Lin x, Lin y	0.82	0.95
	Log x, Log y	0.91	0.92

$$\overline{q_I'^2} = C_{q^2} w_*^2 \left(\frac{g_I}{S_I}\right)^2 c\, R_I^{-1} = C_{q^2}' w_*^2 \left(\frac{g_I}{S_I}\right)^2 \frac{S_I^2}{N_I^2} = C_{q^2}' w_*^2 \left(\frac{g_I}{N_I}\right)^2 \tag{17}$$

which is equation (12). This has a significant implication: The water vapor variance in the IL does not depend on the wind shear in the IL.
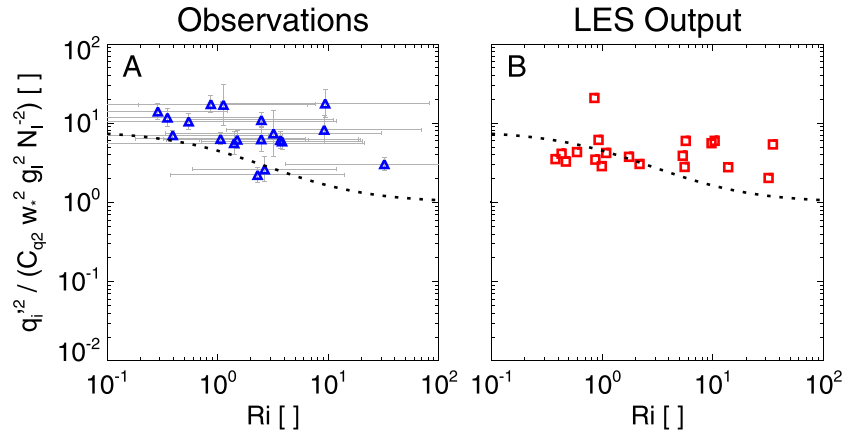
Figure 6. The dimensionless variance ratio (equation (14)) versus the gradient Richardson number using the Sorbjan coefficient of $C_{q2} = 0.08$ for the observations (left-panel) and LES (right panel). The black dotted line is Sorbjan's estimate of $f_{q^2}(R_I)$ using equation (13) and $c_r = 8$. The uncertainties in the observations are denoted with gray error bars. LES = large-eddy simulation.

Figure 8 shows the predicted variance, using equation (17), versus the true variance for the observations and LES output. The general character of the scatterplot for the observations relative to Sorbjan's hypothesized similarity function (equation (8)) is the same; however, the LES results using equation (17) clearly show more consistent agreement with the true variance. Figure 9 shows the true variance divided by the variance predicted using equation (17) and $C_{q2} = 0.55$ versus R_I over a very large range of gradient Richardson number and shows no significant dependence on R_I for either the observations or the LES output.

4.3. Ramifications

The implication that wind shear does not contribute to the water vapor variance in the IL has some important ramifications. First, as water vapor mixing ratio is a conserved tracer, this implies that shear is unimportant when predicting the variance of any other tracer (e.g., other trace gases, and pollutants) in the IL. Second, this suggests that combinations of the scaling variables (equations (1)–(4)) do not need to be modified to account for wind shear. This would imply that a relationship for the water vapor flux in the IL (Q_I) given by equation (9) can be simplified to have $f_Q(R_I) = 1$. Furthermore, this implies that the similarity relationships for temperature variance ($\overline{\theta_I'^2}$), vertical wind variance ($\overline{w_I'^2}$), and entrainment fluxes of momentum
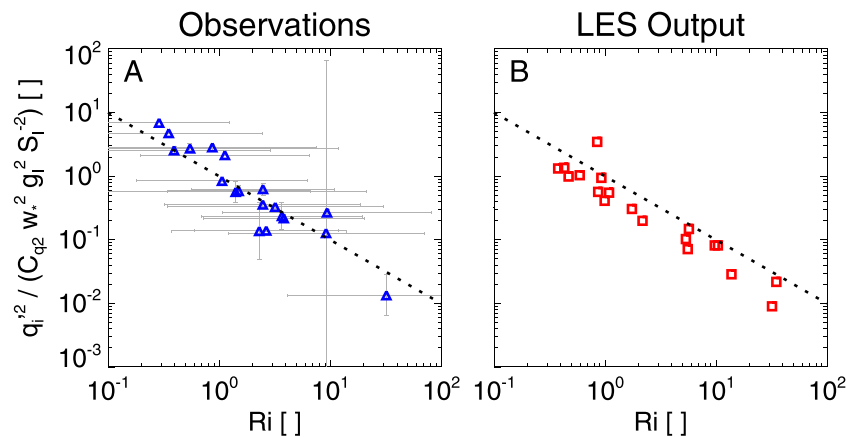

Figure 7. The dimensionless variance ratio (equation (16)) versus the gradient Richardson number using the updated coefficient of $C_{q2} = 0.55$ for the observations (left panel) and LES (right panel). The black dotted line is given by $^1/_{R_I}$. The correlation coefficients for both the (a) observations and (b) large-eddy simulation (LES) output is given in Table 3. The uncertainties in the observations are denoted with gray error bars.
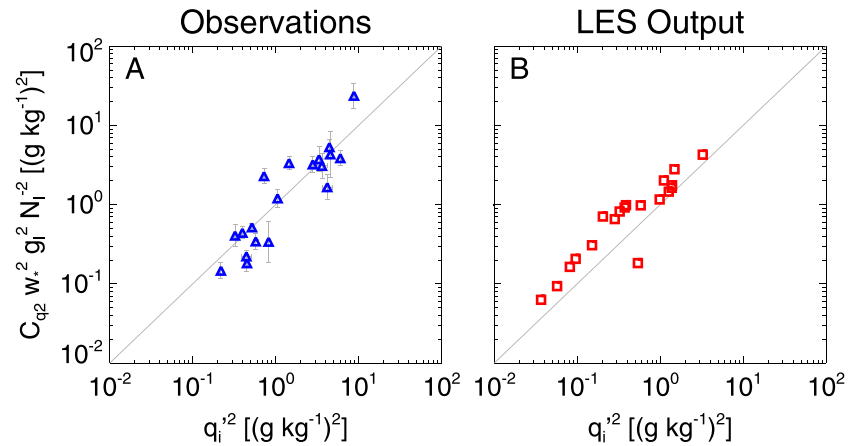
Figure 8. The predicted (using equation (17), which assumes shear has no contribution to the variance) versus true variance for (a) observations and the (b) large-eddy simulation (LES) output. The predicted variance used $C_{q2} = 0.55$. The correlation coefficients for both the observations and LES output is given in Table 3. The uncertainties in the observations are denoted with gray error bars.

(M_I) and temperature (H_I) in the IL given by equations (16), (17), (9), and (10) in Wulfmeyer et al. (2016) could all be simplified to have $f_x(R_I) = 1$.

This result is a bit counterintuitive, as it is seems that shear should play a role in modulating the water vapor variance in the interfacial layer. One possible explanation is that there is significant correlation between the shear and either the water vapor or temperature gradient in the interfacial layer, and thus the effect of shear is being represented by these other variables in the similarity relationship. We would need a larger data set to investigate this well. It is also possible that our selection criteria of identifying quasi-stationary CBLs is eliminating cases with very high shear, as in these events the CBL would move from a buoyancy-driven regime to a mechanically mixed one; but our results do span over 3 orders of magnitude in shear (Figure 4). Furthermore, the uncertainties in the wind shear observations (and hence R_I) are relatively large, and thus the dimensionless variance ratio in Figure 9 may have a slight dependence on the gradient Richardson number.

Regardless, these are hypotheses that need to be tested using advanced datasets such as those collected at the ARM sites, the LAFO site in southern Germany, or during field campaigns such as the Land-Atmosphere Feedback Experiment (Wulfmeyer et al., 2018) where the full instrument complement needed to test these relationships are operating. Additionally, the general stability of the constant C_{q2} in equation (17) for
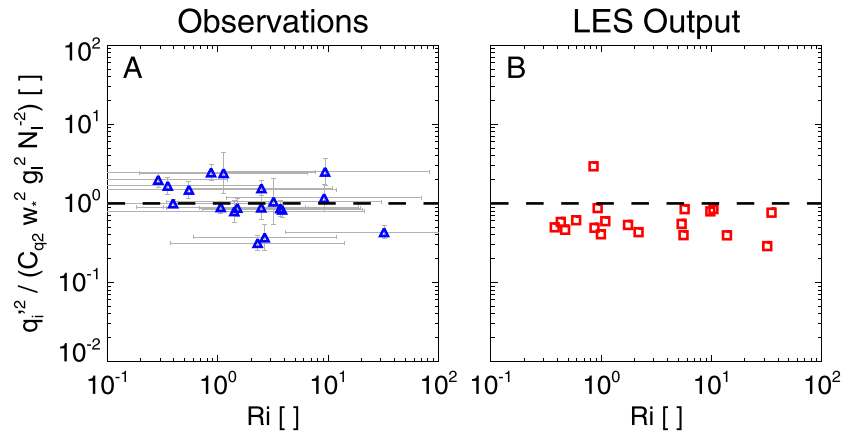

Figure 9. The true variance divided by equation (17) (using $C_{q2} = 0.55$) versus R_I. The observations are shown in the left-panel, with the LES results in the right panel. The uncertainties in the observations are denoted with gray error bars. LES = large-eddy simulation.

different geographic locations and weather regimes, and by extension of the similar constants in the other similarity relationships such as C_Q in the water vapor flux in equation (9), needs to be investigated at other locations.

5. Summary

Similarity relationships are used to estimate higher-order moments and fluxes in numerical weather prediction and climate models from variables that these models predict, such as gradients in temperature, humidity, and wind. We have used remote-sensing observations to evaluate a similarity relationship that predicts water vapor variance in the IL. These observations, together with complementary LES runs that were performed for the same cases, demonstrate that wind shear does not play a significant role in modifying the water vapor variance in the IL. Furthermore, the similarity relationship given by equation (12) is able to reproduce the true variance reasonably well over ~2.5 orders of magnitude.

References

Angevine, W. M., Olson, J. B., Kenyon, J., Gustafson, W. I. Jr., Endo, S., Suselj, K., & Turner, D. D. (2018). Shallow cumulus in WRF parameterizations evaluated against LASSO large-eddy simulation. *Monthly Weather Review*, *146*, 4303–4322. https://doi.org/10.1175/MWR-D-18-0115.1

Atmospheric Radiation Measurement (ARM) (1993). Best-estimate fluxes from EBBR measurements and bulk aerodynamics calculations (30BAEBBR). 2016-02-01 to 2016-08-30, Southern Great Plains (SGP) Lamont, OK (Extended) (E13). Compiled by K. Gaustad and S. Xie. Atmospheric Radiation Measurement (ARM) Climate Research Facility Data Archive: Oak Ridge, TN. Data set accessed 2019-01-26 at https://doi.org/10.5439/1027268

Atmospheric Radiation Measurement (ARM) (1997). Eddy correlation flux measurement system (30ECOR). 2016-02-02 to 2016-09-30, 36.607 N 97.488 W: Southern Great Plains (SGP) Lamont, OK (Extended, secondary) (E14). Compiled by D. Cook. Atmospheric Radiation Measurement (ARM) Climate Research Facility Data Archive: Oak Ridge, TN. Data set accessed 2017-02-07 at https://doi.org/10.5439/1025039

Berg, L. K., Newsom, R. K., & Turner, D. D. (2017). Year-long vertical velocity statistics derived from Doppler lidar in the continental convective boundary layer. *Journal of Applied Meteorology and Climatology*, *56*, 2441–2454. https://doi.org/10.1175/JAMC-D-16-0359.1

Brutsaert, W. H. (1982). *Evaporation in the atmosphere* (pp. 210–212). Dordrecht, Holland: D. Reidel Publishing Company.

Conzemius, R. J., & Fedorovich, E. (2006). Dynamics of sheared convective boundary layer entrainment. Part I: Methodological background and large-eddy simulations. *Journal of the Atmospheric Sciences*, *63*(4), 1151–1178. https://doi.org/10.1175/JAS3691.1

Couvreux, F., Guichard, F., Masson, V., & Redelsperger, J.-L. (2007). Negative water vapour skewness and dry tongues in the convective boundary layer: Observation and large-eddy simulation budget analysis. *Boundary-Layer Meteorology*, *123*(2), 269–294. https://doi.org/10.1007/s10546-006-9140-y

Deardorff, J. W. (1974). Three-dimensional numerical study of turbulence in an entraining mixed layer. *Boundary-Layer Meteorology*, *7*(2), 199–226. https://doi.org/10.1007/BF00227913

Ecklund, W. L., Carter, D. A., & Balsley, B. B. (1988). A UHF wind profiler for the boundary layer: Brief description and initial results. *Journal of Atmospheric and Oceanic Technology*, *5*(3), 432–441. https://doi.org/10.1175/1520-0426(1988)005<0432:AUWPFT>2.0.CO;2

Ferrare, R., Turner, D., Clayton, M., Schmid, B., Redemann, J., Covert, D., et al. (2006). Evaluation of daytime measurements of aerosols and water vapor made by an operational Raman lidar over the Southern Great Plains. *Journal of Geophysical Research*, *111*, D05S08. https://doi.org/10.1029/2005JD005836

Garcia, J. R., & Mellado, J. P. (2014). The two-layer structure of the entrainment zone in the convective boundary layer. *Journal of the Atmospheric Sciences*, *71*, 1935–1955. https://doi.org/10.1175/JAS-D-13-0148.1

Gentine, P., Bellon, G., & van Heerwaarden, C. C. (2015). A closer look at boundary layer inversion in large-eddy simulations and bulk models: Buoyancy-driven case. *Journal of the Atmospheric Sciences*, *72*(2), 728–749. https://doi.org/10.1175/JAS-D-13-0377.1

Golaz, J.-C., Larson, V. E., & Cotton, W. R. (2002). A PDF-based model for boundary layer clouds Part I: Method and model description. *Journal of the Atmospheric Sciences*, *59*(24), 3540–3551. https://doi.org/10.1175/1520-0469(2002)059<3540:APBMFB>2.0.CO;2

Goldsmith, J. E. M., Blair, F. H., Bisson, S. E., & Turner, D. D. (1998). Turn-key Raman lidar for profiling atmospheric water vapor, clouds, and aerosols. *Applied Optics*, *37*(21), 4979–4990. https://doi.org/10.1364/AO.37.004979

Grachev, A. A., Fairall, C. W., & Bradley, E. F. (2000). Convective profile constants revisited. *Boundary-Layer Meteorology*, *94*, 495–515. https://doi.org/10.1023/A:1002452529672

Jiménez, P. A., Dudhia, J., González-Rouco, J. F., Navarro, J., Montávez, J. P., & García-Bustamante, E. (2012). A revised scheme for the WRF surface layer formulation. *Monthly Weather Review*, *140*, 898–918. https://doi.org/10.1175/MWR-D-11-00056.1

Kaimal, J. C., & Finnigan, J. J. (1994). *Atmospheric boundary layer flows: Their structure and measurement*. New York: Oxford University Press.

Lenschow, D. H., Wulfmeyer, V., & Senff, C. (2000). Measuring second-through fourth-order moments in noisy data. *Journal of Atmospheric and Oceanic Technology*, *17*(10), 1330–1347. https://doi.org/10.1175/1520-0426(2000)017<1330:MSTFOM>2.0.CO;2

Liu, C., Fedorovich, E., & Huang, J. (2018). Revisiting entrainment relationships for shear-free and sheared convective boundary layers through large-eddy simulations. *Quarterly Journal of the Royal Meteorological Society*, *144*(716), 2182–2195. https://doi.org/10.1002/qj.3330

Mahrt, L. (1991). Boundary-layer moisture regimes. *Boundary-Layer Meteorology*, *152*(151), 176.

McNicholas, C., & Turner, D. D. (2014). Characterizing the convective boundary layer turbulence with a high spectral resolution lidar. *Journal of Geophysical Research: Atmospheres*, *119*, 12,910–12,927. https://doi.org/10.1002/2014JD021867

Mellado, J. P., Puche, M., & van Heerwaarden, C. C. (2017). Moisture statistics in free convective boundary layers growing into linearly stratified atmospheres. *Quarterly Journal of the Royal Meteorological Society*, *143*, 2403–2419. https://doi.org/10.1002/qj.3095

Nakanishi, M., & Niino, H. (2009). Development of an improved turbulence closure model for the atmospheric boundary layer. *Journal of the Meteorological Society of Japan. Ser. II*, *87*(5), 895–912. https://doi.org/10.2151/jmsj.87.895

Newsom, R. K., Turner, D. D., & Goldsmith, J. E. M. (2013). Long-term evaluation of temperature profiles measured by an operational Raman lidar. *Journal of Atmospheric and Oceanic Technology*, *30*(8), 1616–1634. https://doi.org/10.1175/JTECH-D-12-00138.1

Newsom, R. K., Turner, D. D., Mielke, B., Clayton, M., Ferrare, R., & Sivaraman, S. (2009). The use of simultaneous analog and photon counting detection for Raman lidar. *Applied Optics*, *48*(20), 3903–3914. https://doi.org/10.1364/AO.48.003903

Osman, M. K., Turner, D. D., Heus, T., & Newsom, R. K. (2018). Characteristics of water vapor turbulence profiles in convective boundary layers during the dry and wet seasons over Darwin. *Journal of Geophysical Research: Atmospheres*, *123*, 4818–4836. https://doi.org/10.1029/2017JD028060

Poulos, G. S., Blumen, W., Fritts, D. C., Lundquist, J. K., Sun, J., Burns, S. P., et al. (2002). CASES-99: A comprehensive investigation of the stable nocturnal boundary layer. *Bulletin of the American Meteorological Society*, *83*(4), 555–581. https://doi.org/10.1175/1520-0477(2002)083,0555:CACIOT.2.3.CO;2

Santanello, J. A. Jr., Dirmeyer, P. A., Ferguson, C. R., Findell, K. L., Tawfik, A. B., Berg, A., et al. (2018). Land-atmosphere interactions: The LoCo perspective. *Bulletin of the American Meteorological Society*, *99*(6), 1253–1272. https://doi.org/10.1175/BAMS-D-17-0001.1

Simmer, C., Thiele-Eich, I., Masbou, M., Amelung, W., Bogena, H., Crewell, S., et al. (2015). Monitoring and modeling the terrestrial system from pores to catchments: The transregional collaborative research center on patterns in the soil-vegetation-atmosphere system. *Bulletin of the American Meteorological Society*, *96*(10), 1765–1787. https://doi.org/10.1175/BAMS-D-13-00134.1

Sisterson, D. L., Peppler, R. A., Cress, T. S., Lamb, P. J., & Turner, D. D. (2016). The ARM Southern Great Plains (SGP) site. *The Atmospheric Radiation Measurement (ARM) program: The first 20 years. Meteorological Monographs*, *57*, 6.1–6.14. https://doi.org/10.1175/AMSMONOGRAPHS-D-16-0004.1

Sorbjan, Z. (1996). Numerical study of penetrative and "solid lid" non-penetrative convective boundary layers. *Journal of the Atmospheric Sciences*, *53*(1), 101–112. https://doi.org/10.1175/1520-0469(1996)053<0101:NSOPAL>2.0.CO;2

Sorbjan, Z. (2001). An evaluation of local similarity at the top of the mixed layer based on large-eddy simulations. *Boundary-Layer Meteorology*, *101*(2), 183–207. https://doi.org/10.1023/A:1019260632125

Sorbjan, Z. (2005). Statistics of scalar fields in the atmospheric boundary layer based on large-eddy simulations. Part I: Free convection. *Boundary-Layer Meteorology*, *116*(3), 467–486. https://doi.org/10.1007/s10546-005-0907-3

Sorbjan, Z. (2006). Statistics of scalar fields in the atmospheric boundary layer based on large-eddy simulations. Part II: Forced convection. *Boundary-Layer Meteorology*, *119*(1), 57–79. https://doi.org/10.1007/s10546-005-9014-8

Turner, D. D., Ferrare, R. A., Wulfmeyer, V., & Scarino, A. J. (2014). Aircraft evaluation of ground-based Raman lidar water vapor turbulence profiles in convective mixed layers. *Journal of Atmospheric and Oceanic Technology*, *31*(5), 1078–1088. https://doi.org/10.1175/JTECH-D-13-00075.1

Turner, D. D., Goldsmith, J. E. M., & Ferrare, R. A. (2016). Development and applications of the ARM Raman lidar. *The Atmospheric Radiation Measurement (ARM) program: The first 20 years. Meteorological Monographs*, *57*, 18.1–18.15. https://doi.org/10.1175/AMSMONOGRAPHS-D-15-0026.1

Turner, D. D., Wulfmeyer, V., Berg, L. K., & Schween, J. H. (2014). Water vapor turbulence profiles in stationary continental convective mixed layers. *Journal of Geophysical Research: Atmospheres*, *119*, 11,151–11,165. https://doi.org/10.1002/2014JD022202

van Heerwaarden, C. C., van Stratum, B. J. H., Heus, T., Gibbs, J., Fedorovich, E., & Mellado, J. P. (2017). MicroHH 1.0: A computational fluid dynamics code for direct numerical simulation and large-eddy simulation of atmospheric boundary layer flows. *Geoscientific Model Development*, *10*, 3145–3165. https://doi.org/10.5194/gmd-10-3145-2017

Williams, C. R., Ecklund, W. L., & Gage, K. L. (1995). Classification of precipitating clouds in the tropics using 915-MHz wind profilers. *Journal of Atmospheric and Oceanic Technology*, *12*(5), 996–1012. https://doi.org/10.1175/1520-0426(1995)012<0996:COPCIT>2.0.CO;2

Wulfmeyer, V., Behrendt, A., Sorbian, Z., Turner, D. D., & Hardesty, R. M. (2016). Determination of convective boundary layer entrainment fluxes, dissipation rates, and the molecular destruction of variances: Theoretical description and a strategy for its confirmation with a Novel Lidar System Synergy. *Journal of the Atmospheric Sciences*, *73*, 667–692. https://doi.org/10.1175/JAS-D-14-0392.1

Wulfmeyer, V., Pal, S., Turner, D. D., & Wagner, E. (2010). Can water vapor Raman lidar resolve profiles of turbulent variables in the convective boundary layer? *Boundary-Layer Meteorology*, *136*(2), 253–284. https://doi.org/10.1017/s10546-010-9494-z

Wulfmeyer, V., Turner, D. D., Baker, B., Banta, R., Behrendt, A., Bonin, T., et al. (2018). A new research approach for observing and characterizing land-atmosphere feedback. *Bulletin of the American Meteorological Society*, *99*(8), 1639–1667. https://doi.org/10.1175/BAMS-D-17-0009.1

Xie, S., Cederwall, R. T., & Zhang, M. (2004). Developing long-term single-column model/cloud system—Resolving model forcing data using numerical weather prediction products constrained by surface and top of the atmosphere observations. *Journal of Geophysical Research*, *109*, D01104. https://doi.org/10.1029/2003JD004045